

<https://doi.org/10.1038/s41529-024-00504-3>

Microstructural investigation of Au ion-irradiated Eu-doped LaPO₄ ceramics and single crystals

Check for updates

Sara E. Gilson¹ ✉, Volodymyr Svitlyk^{1,2}, Andrey A. Bukaemskiy³, Jonas Niessen⁴, Theresa Lender⁵, Gabriel L. Murphy³, Maximilian Henkes³, Holger Lippold¹ , Julien Marquardt⁶ , Shavkat Akhmadaliev⁷, Christoph Hennig^{1,2}, Bjoern Winkler⁶, Thorsten Tonnesen⁴, Lars Peters⁵ , Cornelius Fischer¹ & Nina Huittinen^{1,8} ✉

Ceramics and single crystals of LaPO₄ monazite doped with Eu(III) were irradiated with 14 MeV Au⁵⁺ ions at three different fluences. Changes to crystallinity, local coordination environments, and topography were probed using grazing-incidence X-ray diffraction (GIXRD), vertical scanning interferometry (VSI), scanning electron microscopy (SEM), Raman, and luminescence spectroscopy. GIXRD data of the ceramics revealed fluence dependent amorphization. A similar level of amorphization was detected for samples irradiated with 5×10^{13} ions/cm² and 1×10^{14} ions/cm², whereas the sample irradiated with the highest fluence of 1×10^{15} ions/cm² appeared slightly less amorphous. VSI showed clear swelling of entire grains at the highest ion fluence, while more localized damage to grain boundaries was detected for ceramic samples irradiated at the lowest fluence. Single crystal specimens showed no pronounced topography changes following irradiation. SEM images of the ceramic irradiated at the highest fluence showed topological features indicative of grain surface melting. Raman and luminescence data showed a different degree of disorder in polycrystalline vs. single crystal samples. While changes to PO₄ vibrational modes were observed in the ceramics, changes were more subtle or not present in the single crystals. The opposite was observed when probing the local Ln-O environment using Eu(III) luminescence, where the larger changes in terms of an elongation of the Eu-O (or La-O) bond and an increasing relative disorder with increasing fluence were observed only for the single crystals. The dissimilar trends observed in irradiated single crystals and ceramics indicate that grain boundary chemistry likely plays a significant role in the radiation response.

The rare-earth phosphate mineral monazite (LnPO₄, Ln = La-Gd) has been studied extensively due to its interesting properties and use in a variety of applications, ranging from the technological field to the nuclear sector^{1–3}. These compounds are of particular interest for use as nuclear waste forms⁴. Monazite crystallizes in the *P2₁/n* space group and demonstrates notable compositional flexibility as it is able to incorporate the light, trivalent lanthanides La-Gd and form various solid solutions, in addition to the incorporation of divalent ions, such as Ca(II), and tetravalent ions, such as U(IV), through charge-coupled substitution to preserve charge neutrality^{1,5}.

Natural monazite samples are reported to contain up to 20 weight% Th and U, yet do not demonstrate metamictization (radiation-induced amorphization)^{4,6–8}. The high radiation tolerance and structural annealing observed in old natural monazite samples along with the rather low critical amorphization temperature of monazite (350–490 K), above which the structure cannot be amorphized, make it a prominent candidate for the immobilization of actinide elements^{7,9}. Actinides are the fuel of nuclear energy and many are potent α -emitters. As such, actinides recovered from spent nuclear fuel or dismantled nuclear weapons require structurally and

¹Institute of Resource Ecology, Helmholtz Zentrum Dresden-Rossendorf, Dresden, Germany. ²The Rossendorf Beamline at ESRF, The European Synchrotron, Grenoble, France. ³Institute of Fusion Energy and Nuclear Waste Management (IFN-2), Forschungszentrum Jülich GmbH, Jülich, Germany. ⁴Institut für Gesteinshüttenkunde, RWTH Aachen University, Aachen, Germany. ⁵Institut für Kristallographie, RWTH Aachen University, Aachen, Germany. ⁶Institut für Geowissenschaften, Goethe-Universität Frankfurt, Frankfurt am Main, Germany. ⁷Ion Beam Center, Helmholtz Zentrum Dresden-Rossendorf, Dresden, Germany. ⁸Institute of Chemistry and Biochemistry, Freie Universität Berlin, Berlin, Germany. ✉ e-mail: gilsonse@ornl.gov; n.huittinen@hzdr.de

chemically robust matrices with high radiation resistance for proper immobilization^{10–12}.

The response of monazites to irradiation has been reported extensively in the literature. Although natural monazites are not metamict, numerous studies have demonstrated that ion-irradiation of monazites can induce amorphization^{9,13–17}. Additionally, potent α -emitting, polycrystalline actinide monazites $^{241}\text{AmPO}_4$ and $^{238}\text{PuPO}_4$ have been shown to become amorphous due to self-irradiation^{18,19}. Somewhat different results were obtained for monazite single crystals with ^{238}Pu doping. These samples had lower doping of ^{238}Pu and therefore a lower dose rate than an endmember PuPO_4 composition and demonstrated that structural annealing was possible due to sufficient time between successive damage events⁹. This is corroborated by ion irradiation studies, showing that a threshold fluence (or atomic displacements per atom, DPA) is required to amorphize the monazite material. DPA is defined as the number of displacements that occur per atom¹⁷. In contrast, beam-induced annealing has been observed for both electron-irradiated and heavy ion irradiated materials for high particle/ion fluences, suggesting that there is a minimum and a maximum dose rate where amorphization can take place²⁰.

Earlier studies come to conflicting conclusions regarding the long- and short-range structural response of monazite to irradiation. For AmPO_4 , radiation damage in the sample is not homogeneous as both amorphous and nanocrystalline regions were observed with transmission electron microscopy (TEM)¹⁸. In contrast, nuclear magnetic resonance studies of the local coordination environments in this sample demonstrated that the basic monazite structural units, particularly the phosphorous environments, were still intact and that the microstructure of the AmPO_4 sample was not affected¹⁸. In Au and He-ion irradiation studies of monazite samples by ref. 13, radiation damage from electronic and nuclear interactions were probed. Radiation damage effects such as swelling, volume expansion, and X-ray amorphization were observed, whereas Raman spectra indicated that the phosphorus–oxygen bond remained unaffected. Additionally, the authors noted no change in the properties mentioned above after He-ion implantation, suggesting nuclear interactions predominate in the studied dose range¹³. All of these earlier studies underscore that there are different structural responses of various monazite compositions to irradiation. Due to the differing irradiation conditions regarding dose-rate (or fluence), temperature, or ion energies, common factors explaining the different structural responses of natural and synthetic monazite specimens are difficult to pinpoint. In addition, the role of grain boundaries as a sink for point-defects, where defect recombination can occur following irradiation, has been shown in recent studies^{21–24}. Thereby, a different radiation response of polycrystalline samples and single crystals can be expected. However, there is a dearth of studies that focus on how polycrystalline samples and single crystals of the same chemical composition differ in their response to radiation. This is emphasized in the current study.

In this study, we irradiated ceramics and single crystals of LaPO_4 with 14 MeV Au^{5+} ions to simulate the recoil of daughter products that occurs during alpha decay. Samples were cooled with liquid N_2 during irradiation. Although the energy of these incident ions is higher than the energies of recoil nuclei produced during an alpha decay event (100–400 keV), this higher energy allows for deep enough penetration into the samples so that an irradiated layer could be identified and analyzed^{11,25}. The ceramics and single crystals were synthesized from the same rhabdophane parent material so that radiation damage of polycrystalline versus single crystal material could be directly compared. By irradiating targets with the same chemical composition but different sample form, we probed the response to irradiation of individual single crystals and polycrystalline ceramics with grain boundaries. Samples were irradiated at three different fluences selected to induce detectable radiation damage: 5×10^{13} (F1), 1×10^{14} (F2), and 1×10^{15} ions/cm² (F3). The former two fluences are both above the critical amorphization dose for monazite, whereas the latter fluence could result in beam-induced annealing based on earlier studies^{3,16}.

We probed the microstructure of the irradiated layers. Grazing-incidence X-ray diffraction (GIXRD) measurements were used to selectively

probe the top irradiated layer of each ceramic and detect changes in the long-range order and crystallinity of the monazite after irradiation. Irradiation-induced topological and microstructural changes in grain shape and size were investigated with vertical scanning interferometry (VSI) and scanning electron microscopy (SEM). These techniques were complemented by spectroscopic measurement to assess changes in the short-range order and local coordination environments of the monazite samples. Raman spectroscopy allows for the observation of lattice vibrations characteristic of the monazite structure. Changes in the Raman bands (Raman shift, full-width at half-maximum, appearance of new bands) with irradiation can indicate disturbances in the bonding of the structure^{17,26}. Finally, ceramics and single crystals were doped with Eu(III) as a luminescent probe to allow for a local structural analysis by luminescence spectroscopy. By irradiating ceramics and single crystals of the same composition under identical conditions, we examined the dependence of the response to the irradiation on sample form, both in the presence and absence of grain boundaries.

Results and discussion

Synthesis details for the monazite ceramics and single crystals and irradiation details are given in the Methods section and in the supplementary information (SI), sections *Density determination and Irradiation details*, Supplementary Tables 1 and 2, Supplementary Figs. 1–3. A combination of diffraction and spectroscopic techniques was used to confirm that the composition of the ceramics and single crystals were LaPO_4 monazite. A representative diffraction pattern of a pristine, unirradiated monazite ceramic is presented in Supplementary Fig. 4. Additionally, Raman spectra and luminescence spectra of both single crystals and ceramics agree with data reported of corresponding monazite-type samples in the literature^{27,28}.

Irradiation details are included in the Methods section. The Stopping and Range of Ions in Matter (SRIM) Monte Carlo simulation code²⁹ with the “full cascade” option was used to estimate the penetration depth of 14 MeV Au ions into LaPO_4 (Supplementary Figs. 1–3)³⁰. A depth of approximately two micrometers was calculated and considered when performing all analyses of the irradiated samples.

Grazing-incidence X-ray diffraction (GIXRD)

To assess the preservation of long-range order, GIXRD experiments were performed to probe the top layer of the samples where, based on the SRIM calculations, the irradiation damage is expected to occur (see Supplementary Figs. 2 and 4). A suitable alignment of the LaPO_4 single crystals with respect to the incident grazing beam was not possible due to their irregular shapes. Therefore, GIXRD data were collected only for dense ceramics of LaPO_4 . An example of an irradiated pellet is shown in Supplementary Fig. 5. As expected, pristine LaPO_4 ceramics were found to be fully crystallized (Supplementary Fig. 6). In contrast, the data from irradiated pellets were dominated by diffuse scattering, although reflections from crystalline phases could still be observed in all the samples, even those treated with the highest fluences (Fig. 1). The signal obtained from the crystalline phases present in the irradiated samples is very similar to the signal obtained from the non-irradiated sample (Fig. 1a, b). Specifically, peaks have the same peak shape and broadening. Therefore, Bragg peaks present in the irradiated samples can be attributed to the pristine component not affected by irradiation. Note, some Bragg reflexes are missing, due to the absence of diffracting grains at the probed region of the very textured ceramic pellets. All present diffraction peaks can be assigned to LaPO_4 monazite, i.e. the samples do not contain impurity phases. A residual fraction of the parent crystalline phase in the irradiated samples can be estimated by comparing relative intensities of the same peak series. In the case of the sample irradiated at the lowest fluence (5×10^{13} ions/cm², F1) (Fig. 1c), the corresponding fraction of the residual parent phase is on the order of 10–15%.

The LaPO_4 sample irradiated at the intermediate fluence (1×10^{14} ions/cm², F2) features similar fractions of amorphous and crystalline phases as the sample irradiated at the F1 fluence (Fig. 1c). The sample treated with the F3 ion fluence (1×10^{15} ions/cm²) shows a slightly weaker contribution from the amorphous part (Fig. 1c) and,

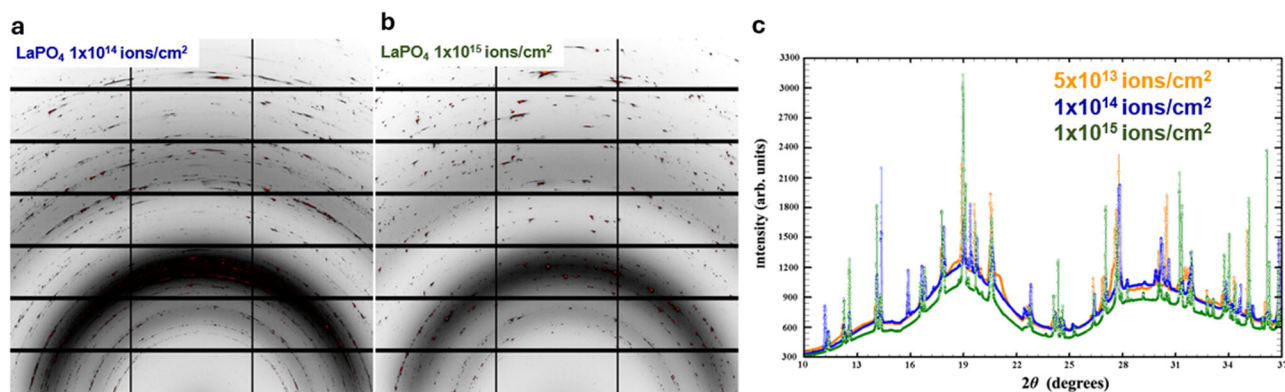
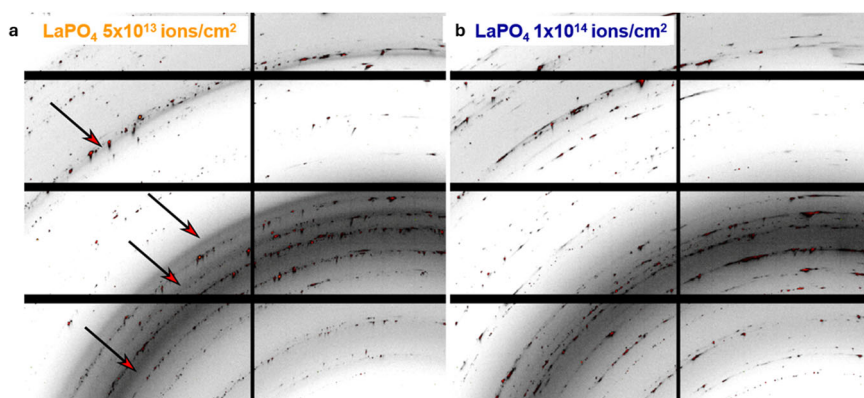


Fig. 1 | GIXRD data for LaPO_4 collected at incident angle $\alpha = 1^\circ$. Diffraction data of the LaPO_4 sample irradiated at F2 (a); sample irradiated at F3 (b); and comparison of the integrated data for samples irradiated at all fluences at incident angle $\alpha = 1^\circ$ (c).

Fig. 2 | Comparison of diffuse scattering of irradiated LaPO_4 ceramics. **a** Scattering from the sample irradiated at F1 featuring structured diffuse scattering on top of broad diffuse signal. **b** Scattering from the sample irradiated at F2 showing only broad diffuse signal.



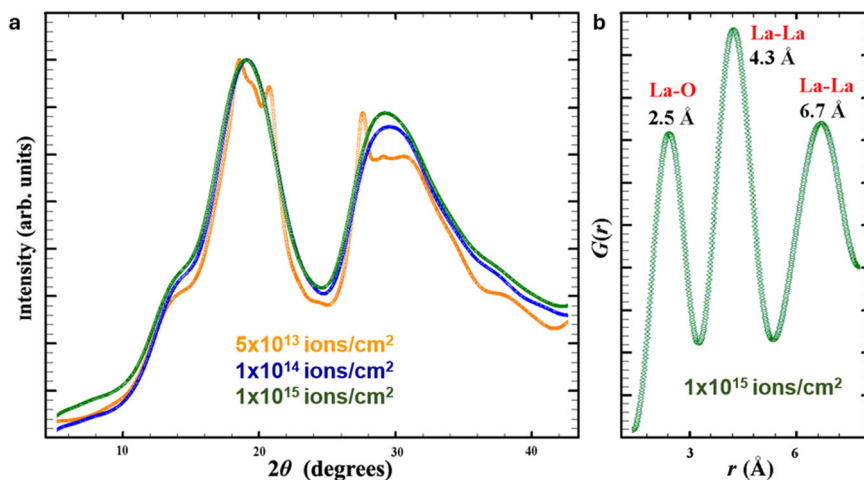
consequently, exhibits a somewhat higher fraction of crystalline phase compared to the samples irradiated with the F1 and F2 fluences. It is known that irradiation with swift heavy ions increases the temperature of the target material *via* generation of local temperature spikes^{31,32}. This in turn can affect the microstructural and structural properties of the irradiated materials. For example, it can cause an increase in grain size or even induce structural transformations^{33,34}. While the irradiated samples in this study were kept at 77 K with liquid N_2 during irradiation, it is not excluded that short (ps time scale) thermal spikes (up to 10^4 K)³¹ may still induce local and rather limited annealing. Indeed, an increase in the effective fluence from F1 to F3 is expected to increase the local thermal load inside the irradiated pellets under the same cooling conditions with a possible influence on the local microstructure, *i.e.* partial stabilization of the parent crystalline phase. During GIXRD experiments, the penetration depth of the X-rays strongly depends on the incident angle, α . Here, $\alpha = 1^\circ$ which corresponds to a penetration depth of ~ 0.42 μm (Supplementary Fig. 7). This value was calculated using the GIXA package^{35–37}. While the theoretical penetration depth of 14 MeV Au^{5+} ions into the LaPO_4 material was estimated to be 2 μm using SRIM²⁹ (see Supplementary Table 2), the parent crystalline phase can already be observed at a low grazing angle $\alpha = 1^\circ$. Conventionally, the penetration depth is defined as the depth at which the intensity of the incoming radiation is reduced to $1/e$ ($\sim 37\%$) of the original intensity at the surface. Using the $1/e$ law, the fraction of the synchrotron beam that can penetrate 2 μm into LaPO_4 is found to be close to 1%. Although this number may seem negligible, 1% out of typical synchrotron flux of $\sim 10^{13}$ photons/s available at the ROBL³⁸ still may produce a signal that is orders of magnitude higher than that obtained with a laboratory source. Therefore, a small amount of strongly diffracting pristine crystalline LaPO_4 may provide a significant

contribution to the experimental data dominated by weak diffuse scattering of amorphized LaPO_4 ³⁹.

A closer look at the scattering data of the irradiated LaPO_4 ceramics reveals that the diffraction pattern from the sample irradiated at the lowest fluence of 5×10^{13} ions/ cm^2 features a few diffuse maxima present on top of the broad diffuse base signal (Fig. 2a). This is in contrast with the diffuse signal from the samples irradiated at the intermediate (Fig. 2b) and highest fluences which exhibit only broad diffuse signals. Careful masking of Bragg reflections on the F1, F2 and F3 ceramics scattering data with a subsequent smoothing of the profile allowed us to obtain qualitative reduced signal from the amorphized part of the irradiated LaPO_4 samples (Fig. 3a). Samples irradiated at the intermediate and highest fluences, F2 and F3 respectively, feature near identical diffuse signals; two broad peaks around 20 and 30° 2θ (Fig. 3a) with a low-angle shoulder on the 20° peak. As mentioned above, the diffraction pattern of the sample irradiated with the lowest fluence displays features in addition to the base diffuse scattering signal observed for the middle F2 and highest F3 fluences (Fig. 3a). The presence of these additional well-defined diffuse features indicates that the amorphous LaPO_4 phase retains more structured short-range order correlations after irradiation at the lowest F1 fluence compared to irradiation at the higher F2 and F3 fluences. Consequently, the higher F2 and F3 fluences induce a higher degree of amorphization of the parent crystalline LaPO_4 phase.

Information on short-range order correlations can be obtained from diffuse scattering experiments by calculating the pair-distribution function (PDF). In this study PDFs, $G(r)$, were calculated with the PDFGetX3 package⁴⁰. The analysis of the LaPO_4 diffuse scattering signal is limited due to the low accessible Q range up to 4.44 \AA^{-1} . Indeed, experiments in GI mode require utilization of low photon energies in order to limit the penetration depth. In contrast, a high photon energy is required to collect high- Q data suitable for a PDF analysis. Nevertheless, three strong peaks can be seen on the experimental $G(r)$ function (Fig.

Fig. 3 | Extracted amorphous scattering signal. Normalized qualitative amorphous scattering signal from the irradiated LaPO₄ ceramic samples, low-*r* part of pair distribution function (a), *G*(*r*), obtained from the ceramic irradiated at F3 scattering data (b).



3b, F3 irradiated sample is shown as an example) and they correspond to scattering pairs with c.a. 2.5, 4.3, and 6.7 Å distances. The origin of these correlations can be determined by examining the three-dimensional crystal structure of the parent crystalline LaPO₄ phase.

At ambient conditions the LaPO₄ phase adopts the monazite-type structure. In standard setting it corresponds to the *P2₁/n* space group and cell parameters of *a* ~ 6.8 Å, *b* ~ 7.1 Å, *c* ~ 6.5 Å, β ~ 103.3°. It consists of edge-sharing LaO₉ and PO₄ polyhedra that form chains along the crystallographic *a* axis (Supplementary Fig. 7). It can be seen that the peak around 2.5 Å on the *G*(*r*) plot corresponds to the average La-O distance in the LaO₉ polyhedra. The 4.3 Å peak corresponds to the closest La-La distances along the *c* direction. The third peak at 6.7 Å matches the *a* unit cell parameter of LaPO₄ and, therefore, originates from La-La distances along the [1 0 0] crystallographic direction mediated by the PO₄ tetrahedra (Supplementary Fig. 8). Consequently, the presence of peaks on the *G*(*r*) function at 2.5 and 6.7 Å indicates the preservation of the LaO₉ polyhedra and stronger structural rigidity along the *a* axis, which is the direction of edge sharing LaO₉ and PO₄ units. In addition, stacking of the LaO₉-PO₄ chains is also correlated by a 4.3 Å peak on the experimental PDF analysis. Since the sample irradiated at the F1 fluence possesses additional features on top of the base diffuse signal observed for the higher F2 or F3 irradiated samples, the lower fluence induces smaller structural damage in LaPO₄, as expected. It may, for instance, indicate better preservation of the LaO₉ structural units which feature nine independent La-O distances in the parent crystalline LaPO₄. However, the corresponding fine details cannot be obtained from the limited scattering data of the F1 irradiated sample.

Vertical scanning interferometry (VSI) and Scanning electron microscopy (SEM)

VSI images were taken of select LaPO₄ monazite ceramics and single crystals (Fig. 4). VSI is a powerful technique for probing a surface topography at the nanoscale to observe features such as surface roughness and grain height^{41,42}. Fig. 4a shows the surface of the monazite ceramic irradiated at the lowest fluence. The primary feature is the swelling that is concentrated at the grain boundaries of the ceramic. In contrast, at the highest fluence (Fig. 4b), the swelling of entire grains is observed, instead of being concentrated at the boundaries of the grain. However, the damage across the irradiated region is not uniform, as smooth areas surround swollen grains. For further comparison, VSI images of the boundary between pristine and irradiated regions of ceramics are given in Supplementary Figs. 9 and 10. For individual monazite single crystals where grain boundaries are not present, no topographical changes are observed between the pristine single crystal (Fig. 4c) and an irradiated one (Fig. 4d).

SEM images were taken of the irradiated ceramics to further probe changes in surface topography due to ion-irradiation. Due to the unevenness and inhomogeneity of the surfaces of the single crystals, SEM images

that clearly resolved the surface features could not be obtained. Representative images of the ceramics irradiated at the highest and lowest fluences are shown in Fig. 5. Energy dispersive spectroscopy (EDS) (Supplementary Figs. 11 and 12) and additional SEM images (Supplementary Figs. 13–50) have been compiled in the SI. Results from EDS analyses are summarized in Supplementary Tables 3–7. The surface of the ceramic irradiated at the highest fluence (F3) exhibits significant damage as observed in Fig. 5a–c. Grain breakage from the surface of the irradiated side of the ceramic signifies severe topographical damage. At the border between the pristine and irradiated parts of the ceramic, differences in grain height indicate that the irradiated side is swollen. Enlarged grains with visible grain boundaries and even grain breakout in the irradiated region of the ceramic are also observed (Supplementary Figs. 39 and 40). The circles on the irradiated surface may be nucleation sites from the ion irradiation (Fig. 5b). It is important to note that the signs of irradiation damage are not uniform across the sample surface, as was observed in TEM studies of AmPO₄¹⁸. In another irradiated region, grains appear smooth as if their surface has melted, with less well-defined grain boundaries and rounded edges (Fig. 5c).

A study by Meldrum et al. reported that irradiation appeared to enhance diffusion and crystallization processes^{9,43}. Additionally, an activation energy of 0.064 eV of recrystallization was calculated, which corresponds to a temperature of about 470 °C⁴³. It is also worth noting that thermal spikes, caused by the transfer of energy of the implantation ions to the electrons in the target material, can cause local heating in the sample⁴⁴. This could also account for possible recrystallization processes in the irradiated monazite samples, as the critical temperature of monazite is between 350 and 485 K⁹. Also, a study of electron-irradiation of monazite by ref. 15 reported recrystallization, even under mild conditions. Studies suggest this ‘alpha annealing’ is dependent on the ratio of energies of electronic to nuclear interactions, however more studies are needed to confirm these findings^{15,20}. This corroborates signs of recrystallization observed in the LaPO₄ ceramic irradiated at the highest fluence. Notably, this phenomenon was not observed in the other two monazite ceramics irradiated at lower fluences.

The ceramic irradiated at the intermediate fluence (F2) exhibited signs of irradiation damage less severe than the ceramic irradiated at the highest fluence. SEM images showed signs of swelling and disintegration of the surface (Supplementary Figs. 22–35). Again, the irradiation damage is not the same across the entire surface. Other irradiated regions of the ceramic are rough compared to the pristine regions, and spalling of the surface is evident. Finally, the ceramic irradiated at the lowest fluence (F1) shows the least damage due to irradiation of all the ceramics. The irradiated regions are rough and exhibit a thin, highly porous surface layer (Fig. 5e). As with the other two ceramics, the irradiation damage does not appear the same throughout the irradiated surface. Differences in grain height and breakouts of grains from the surface are suggested by both VSI and SEM data and suggest radiation-induced swelling (Fig. 5f), as has

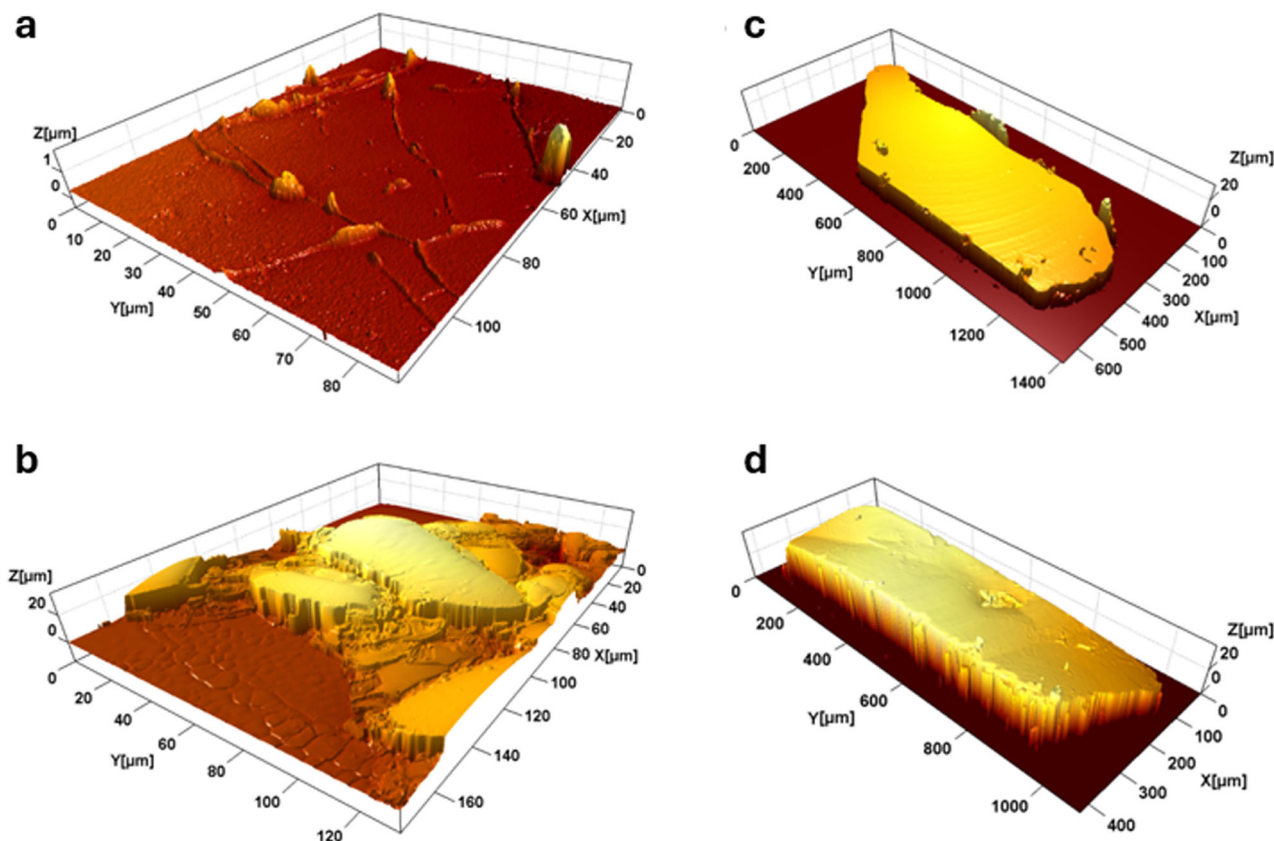


Fig. 4 | VSI images of LaPO_4 monazites. VSI images of LaPO_4 monazite ceramics exposed to F1 (a) and F3 (b) and of single crystals without irradiation (c) and exposed to F3 (d).

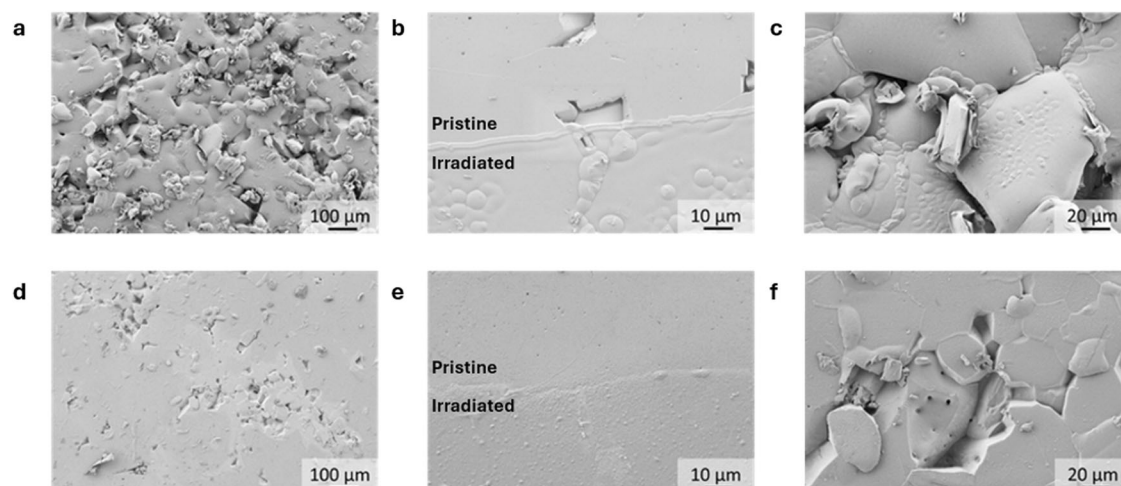


Fig. 5 | SEM images of irradiated LaPO_4 ceramics. SEM images of irradiated LaPO_4 ceramics, the surface of ceramic irradiated at F3 (a), the irradiated-pristine boundary of the ceramic irradiated at F3 (b), grain irradiated at F3 (c), surface of ceramic

irradiated at F1 (d), the irradiated-pristine boundary the ceramic irradiated at F1 (e), and a grain irradiated at F1 (f).

been reported previously^{13,15}. Fig. 5f also shows visible, rather large pores in one of the grains, which are clearly larger in size than pores found on the pristine side of the ceramic pellets (visible in e.g. Fig. 5d (top) and 5e (top)). SEM images indicate that the structural response to irradiation damage is influenced by topology and that the presence of grain boundaries likely plays a role in mediating the effects of the ion irradiation^{33,45}. This could explain the difference in spectroscopic results between the irradiated monazite single crystals and ceramics discussed in the following section.

Raman spectroscopy

Raman spectroscopic measurements of irradiated samples were used to probe changes in local coordination environments of the ceramics and single crystals. It is likely that the laser penetrated into the samples beyond the ~ 2 micron irradiated layer, giving non-negligible contributions from the pristine, unirradiated layers below²⁶.

The Raman spectra of both ceramic samples and single crystals show the appearance of a shoulder on the ν_1 peak (symmetric stretch vibration) at $\sim 960 \text{ cm}^{-1}$ upon irradiation of the samples (Fig. 6). This is observed in both

Fig. 6 | Raman spectra of pristine and irradiated LaPO₄ monazites. Raman spectra of pristine and irradiated LaPO₄ monazite ceramics (a) and single crystals (b).

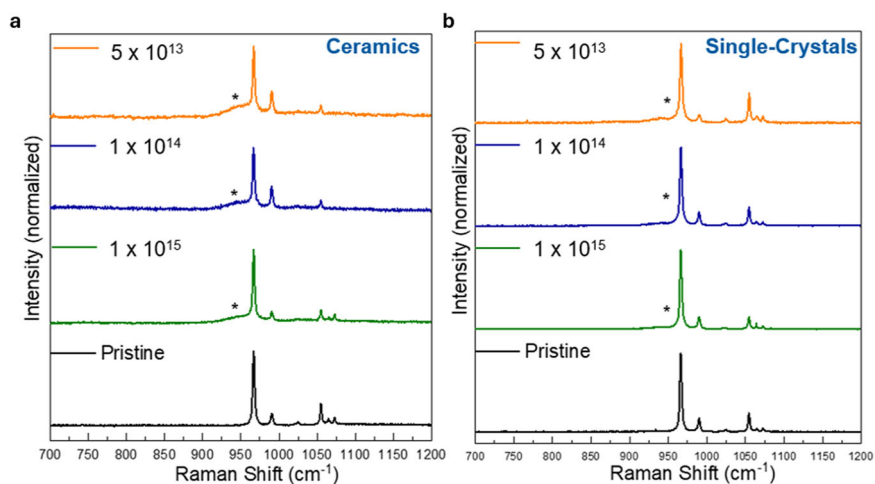
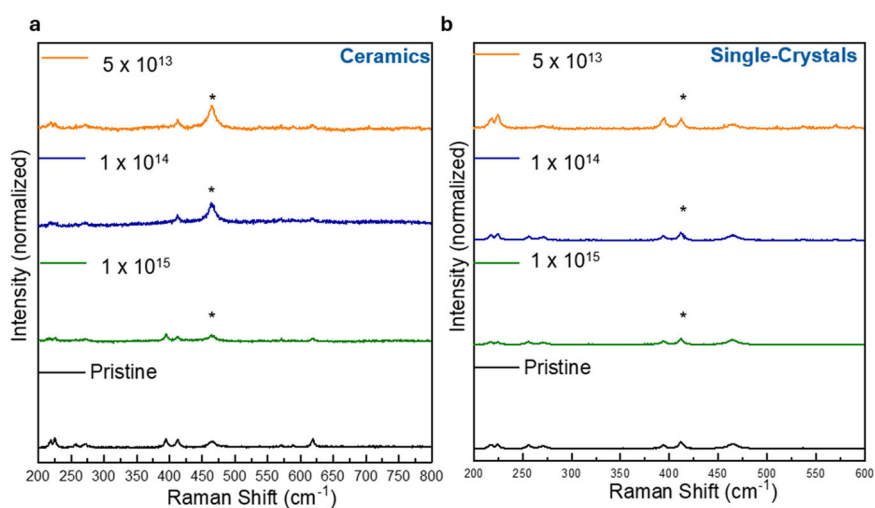


Fig. 7 | Normalized Raman spectra. Raman spectra normalized to the ν_1 band intensity (lower wave-number region) of the irradiated LaPO₄ monazite ceramics (a) and single crystals (b).



the ceramics and single crystals, although it is more pronounced in the Raman spectra of the irradiated ceramics. These spectra demonstrate a disruption in the local coordination environment of these samples, however, the Raman bands characteristic of the monazite structure are still readily observed¹⁴. Interestingly, when Raman data were collected of pores on the surface of the ceramic or in regions close to grain boundaries, the spectra were featureless and indicated amorphization (see Supplementary Fig. 51). This suggests that the damage is concentrated at the grain boundaries in the ceramics. In addition, swollen grains show a larger contribution of the shoulder at 960 cm⁻¹ than smooth surfaces, which speaks for a heterogeneous damage or damage distribution in the ceramics. Similar, clear differences in the collected Raman spectra are not seen for the single crystals, implying a more homogenous (albeit small) overall damage in these specimens (Supplementary Fig. 51).

Additionally, in the ceramic samples, the ν_2 band at ~465 cm⁻¹ increases in intensity with decreasing fluence for the ceramic samples, whereas no clear trend is observed for the single crystals (Fig. 7). This Raman band is attributed to a bending mode of the phosphate tetrahedra^{27,28}. For the monazite ceramics, the ratio of intensities of the ν_2 to ν_1 modes, averaged over multiple Raman spectra from different spots on the sample surfaces, were found to increase with decreasing fluence, as shown in Fig. 7a. This same trend was not observed in the ν_2 to ν_1 ratios of the monazite single crystals (Fig. 7b), however it is worth noting that numerous factors affect the peak intensities in Raman spectra in single crystal studies, especially sample orientation⁴⁶. A study from ref. 47 posits that the intensity of this peak

associated with the phosphate bending mode is dependent on the $Lm:P$ ratio and that intensity decreases with decreasing $Lm:P$ ratios⁴⁷. Finally, the small Raman bands at ~1065 cm⁻¹ and 1073 cm⁻¹, visible in the pristine sample and the LaPO₄ ceramic subjected to the highest fluence (F3), are absent in both samples irradiated at the lower fluences. These bands have been assigned to internal stretching vibrations of the PO₄ tetrahedra¹⁴. Their absence at lower fluences is another indication for the partial recrystallization of the monazite at the highest fluence, which corroborates the results obtained in our diffraction investigations and the SEM micrographs.

Many discrepancies exist in the literature for Raman measurements of irradiated monazites. For example, in studies of Ce-monazite lamellae irradiated using three different Au ion energies, Raman measurements demonstrated substantial structural damage to short-range order indicated by a loss of intensity and shifting of Raman bands to lower wavenumbers^{17,26}. However, other reports of Au-ion irradiated monazite ceramics showed no significant broadening or shifting of the Raman bands, especially those associated with the PO₄ tetrahedra coordination environments¹³. Raman measurements of AmPO₄ polycrystalline samples showed an increase in the full-width at half maximum (FWHM) of certain peaks, such as the band associated with the symmetric stretch of the phosphate tetrahedra, however peak positions remained unchanged¹⁸. It is worth noting that Raman spectra of irradiated monazites appear dependent on a number of factors, such as sample form, type of irradiation (self-irradiation versus external ion-irradiation), and the setup of the Raman instrument as confocal or non-confocal.

Fig. 8 | Eu(III) excitation spectra of LaPO₄ monazites. Eu(III) excitation spectra (${}^7F_0 \leftarrow {}^5D_0$ transition) of LaPO₄ monazites doped with 500 ppm Eu(III): polycrystalline ceramics (a) and single crystals (b).

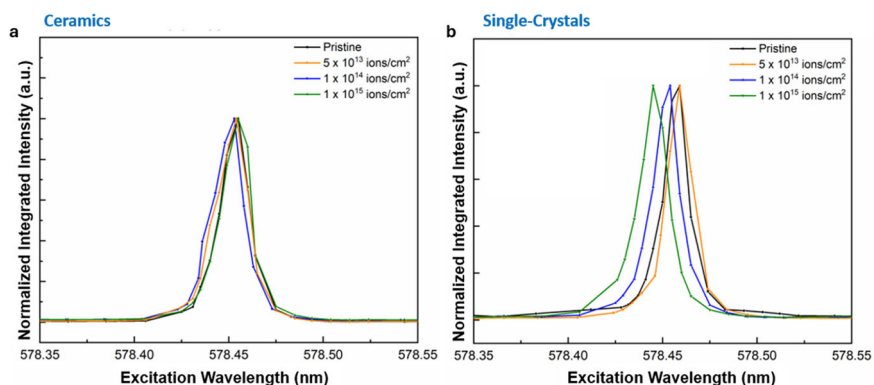
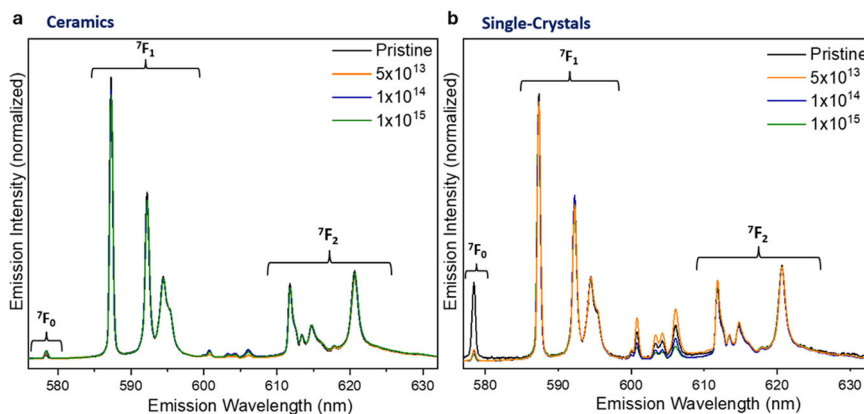


Fig. 9 | Eu(III) emission spectra of irradiated LaPO₄ monazites. Emission spectra of irradiated LaPO₄ monazite ceramics (a) and single crystals (b) doped with 500 ppm Eu(III).



Luminescence spectroscopy

As mentioned previously, all ceramics and single crystals were doped with ~500 ppm Eu(III). Eu(III) is a luminescent lanthanide that is known to be incorporated into the LaPO₄ monazite structure and gives distinctive luminescence spectra that provide information about its local coordination environment⁴⁸. The low concentration of the Eu-dopant was used to avoid self-quenching of the luminescence signal due to two luminescent ions being in close proximity to one another as well as to study how the LaPO₄ end-member and not a La_xEu_{1-x}PO₄ solid solution reacts to heavy ion-irradiation⁴⁹.

Luminescence data include excitation and emission spectra, as well as luminescence lifetime decay plots, which can be used to determine the number of non-equivalent sites in a given matrix, their respective site symmetry, and the lifetimes of each species^{48–50}. It is important to note that luminescent probes, such as Eu(III), still give a spectrum even when in amorphous environments, making it well-suited for a sample in which irradiation-induced amorphization is likely to occur.

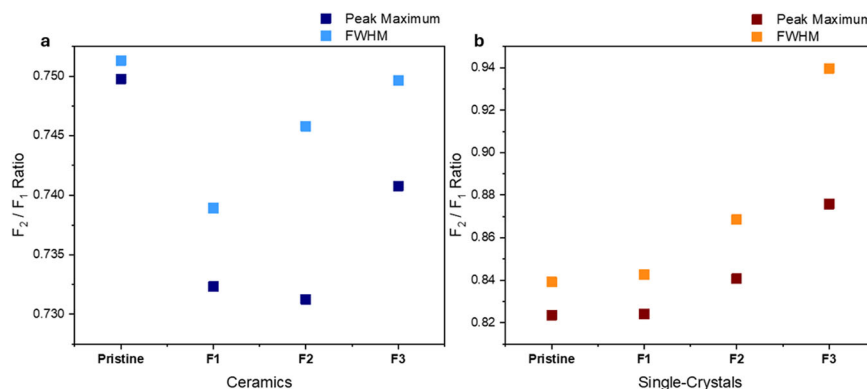
The integrated excitation spectra, i.e. the luminescence emission intensity as a function of excitation wavelength, of irradiated monazite ceramics and single crystals normalized to maximum intensity are presented in Fig. 8. The excitation peak maximum for Eu(III)-doped LaPO₄ has been shown to occur at 578.40 nm^{49,50}. The excitation peak maxima for each of the ceramic and single crystal samples studied here agrees well with this reported value for pristine monazite. For the irradiated samples, the trends in peak maximum relative to each other are different for the two different sample types. For the ceramics, no systematic trend in peak maximum as a function of fluence is observed (Fig. 8a). The peak maxima of the samples irradiated at the F1 and F2 fluences are both slightly blue-shifted compared to that of the pristine sample. A blue-shift has been reported for lanthanide monazite endmembers and solid solutions of La-Gd monazites, where the shift to higher energies in both cases was attributed to the lengthening of the Ln-O bond and the weaker exertion of the ligand field on

the Eu(III) dopant cations^{49,50}. Thereby, analogous to these studies, we assign the minor blue shift in these ceramic samples to a slight increase in the Eu(III)/La-O interatomic distance^{49,50}. The sample irradiated at the highest fluence has a peak maximum almost identical to that of the pristine, suggesting a similar crystal field strength in both samples types, and consequently a very similar Eu(La)-O interatomic distance, compared to the samples irradiated at the lower fluences. This is similar to the findings of the SEM images, in which the surface of the sample irradiated at the highest fluence appeared recrystallized and less damaged. Unlike the ceramics, the integrated excitation spectra show a different trend for the monazite single crystals (Fig. 8b). There is a systematic blue-shift with increasing fluence, again corresponding to an increased interatomic distance between the La atoms and the coordinating oxygen atoms. Spectra of a Ne calibration lamp were taken before the measurement of each sample and confirmed that these shifts, while small, are significant (Supplementary Fig. S2).

The difference in excitation spectra between irradiated monazite ceramics and single crystals could be due to the presence or absence of grain boundaries. Studies have demonstrated that at elevated irradiation temperatures, more defect recombination will occur, but at lower temperatures of irradiation, migration of defects to sinks, such as grain boundaries is more prominent^{44,51}. Additionally, studies have suggested that grain boundaries can act as sinks for point-defects, allowing for defect recombination^{21–24}.

Emission spectra of all samples are presented in Fig. 9. In an unirradiated monazite matrix with monoclinic C₁ lattice symmetry, the Eu(III) dopant cations occupy low symmetry sites that give threefold splitting of the 7F_1 band and fivefold splitting of the 7F_2 band⁴⁸. In this low symmetry system, the ${}^5D_0 \rightarrow {}^7F_1$ transition has predominantly magnetic dipole character and therefore does not change significantly with disturbances in ligand environment⁴⁸. Conversely, the ${}^5D_0 \rightarrow {}^7F_2$ transition has predominantly electric dipole character and is hypersensitive to changes in ligand environment. The typical splitting pattern observed in LaPO₄ monazite doped with 500 ppm Eu(III) is observed in all samples here regardless of sample

Fig. 10 | Trends in the ${}^7F_2/{}^7F_1$ ratios. Trends in the ${}^7F_2/{}^7F_1$ ratios of emission spectra collected after excitation at the peak maximum and at the full width at half maximum of the integrated excitation peaks for the ceramics (a) and the single crystals (b).



type and radiation dose. However, band intensity and sharpness change with fluence.

Changes in the 7F_1 and 7F_2 bands in the ceramics and single crystals with irradiation are subtle. To probe for asymmetry in the coordination environment of the Eu(III) dopant cations, the ${}^7F_2/{}^7F_1$ ratios were calculated both for the emission spectra collected after excitation at the corresponding excitation peak maxima of each sample (these emission spectra are shown in Fig. 9) as well as at the FWHM (see Supplementary Fig. 53 for more details). As broadening of excitation peaks should increase with increasing disorder in the sample, the ${}^7F_2/{}^7F_1$ ratios should be larger at the FWHM than at the excitation peak maximum. These results are given in Fig. 10. For the ceramics, no clear trend in the F_2/F_1 ratio of the irradiated samples is observed when compared to that of the pristine ceramic. All ${}^7F_2/{}^7F_1$ ratios lie between 0.73 and 0.75, and no conclusions of the relative asymmetry can be drawn from these ratios. However, in the case of the single crystals, the F_2/F_1 ratios increase systematically from 0.84 to 0.94 with increasing fluence, corresponding to an increase in asymmetry of the Eu dopant coordination environment. This difference in the F_2/F_1 ratios appears dependent on sample form, again suggesting that grain boundaries in the ceramics affect radiation response. However, the ${}^7F_2/{}^7F_1$ ratio is lower for the emission spectra corresponding to the peak maximum of integrated excitation energy, compared to that of the emission spectra corresponding to the FWHM for all samples, regardless of sample form. This corresponds to more structural disorder and a greater contribution of the irradiated layer in the spectroscopic signal.

Lifetimes were collected for the LaPO_4 monazite ceramics and single crystal samples and correspond to values reported previously in the literature (Supplementary Fig. 54, Supplementary Table 7)⁴⁹. However, the lifetimes of the samples do not provide additional information about their microstructure, specifically with regard to radiation damage. Additional details are offered in the SI.

Summary

In the present study, ion-irradiated LaPO_4 monazite ceramics and single crystals have been investigated with a combination of diffraction, microscopic, and spectroscopic methods. GIXRD data indicated a non-systematic amorphization of the ceramic surface with increasing ion fluence. The extracted reduced signal from the amorphized part of the irradiated LaPO_4 samples featured near identical diffuse signals characterized by two broad peaks around 20 and 30° 2 θ . Detailed information about the short-range order correlations in the sample was obtained from the calculated PDF. Three dominant interatomic distances at ~2.5, 4.3, and 6.7 Å, corresponding to average La-O and La-La distances along the *c* and *a* directions in the monazite structure, respectively were obtained, clearly showing that short-range order is retained in the amorphous material.

VSI and SEM data showed different types of topographical and microstructural damage at the different fluences. At fluence F1, localized damage at the grain boundaries of the ceramic pellet was evidenced, while an increasing fluence resulted in additional grain break out, swelling, and even

softened grains with rounded edges, indicative of grain melting or partial recrystallization of the ceramic surface. Monazite single crystal specimens, on the other hand, showed no topological features following irradiation, attributed to the lack of grain boundaries in the samples.

Raman spectroscopy probing phosphate vibrations in the samples and Eu(III) luminescence spectroscopy addressing the Ln-O environment in the monazites were conducted for the ceramic pellets and single crystal specimens, to understand the relative radiation response of the different sample types. In the Raman spectra of irradiated ceramic samples and single crystals, a shoulder on the symmetric stretch vibration at ~960 cm^{-1} was visible. For ceramic pellets, swollen grains showed a larger contribution of the shoulder at 960 cm^{-1} than smooth surfaces, while grain boundary regions showed featureless spectra indicative for amorphization, which speaks for a heterogeneous damage distribution in the ceramics. In contrast, no differences in the Raman data collected at different regions on the single crystals were seen, implying a more homogenous overall damage in these specimens.

The Eu(III) luminescence data collected for the ceramic samples were almost identical for all fluences. Very small changes in the excitation peak position and the ${}^7F_2/{}^7F_1$ band ratio could be seen for fluences F1 and F2, while spectra collected for F3 were almost identical to the pristine sample. For single crystals on the other hand, a subtle but systematic blue-shift of the excitation peak signal was seen, following an increased interatomic distance between the Eu (La) atoms and the coordinating oxygen atoms with increasing fluence. The increasing bond distance was accompanied by a systematic increase of the ${}^7F_2/{}^7F_1$ band ratio, suggesting an increasing asymmetry in the samples.

The results of this study clearly show that single crystals and ceramics react differently to heavy ion irradiation. While fluence F3 shows large microstructural changes, diffraction and spectroscopic data suggest partial recrystallization of the sample, and a heterogeneous damage distribution localized at grain boundaries. Single crystals without boundaries, show a homogenous damage response, which, especially for the LaO_9 polyhedron, increases with increasing fluence.

As reason for the different damage response of the polycrystalline samples and single crystals, we postulate partial beam-induced annealing of the radiation damage, enabled by grain boundaries where defect recombination can take place. However, defect annealing appears to apply mainly to the La-O environment probed via luminescence spectroscopy, where no changes to the EuO_9 (LaO_9) polyhedron could be observed at the highest fluence. Raman data show amorphous regions at grain boundaries and larger damage to swollen grains than at smooth surfaces, which would imply that similar annealing of the covalent P-O network does not take place to the same extent. However, additional studies targeting annealing mechanisms in irradiated solids are required for an in-depth understanding of the damage-recovery pathways in the monazite LnO_9 and PO_4 polyhedra. For this aim, swift heavy ion irradiation, in which the implantation ions have significantly higher energies and therefore penetrate deeper into the sample could be beneficial, to avoid contributions from the pristine layers of the

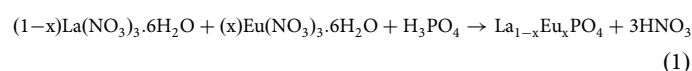
sample during analyses. With this, structural damage such as amorphization and bond elongation, will be more readily observed in diffraction and spectroscopic data.

Finally, this study underlines the necessity to consider the correct sample type and design when investigating irradiation damages of materials for nuclear waste disposal. For monazites, irradiation results obtained for single crystals are not necessarily directly transferable to ceramic specimens, which should thereby, always be included in irradiation studies to understand the radiation response of a ceramic waste form in high radiation fields.

Methods

Synthesis methods

Fabrication of LaPO₄ ceramics. The synthesis method for the LaPO₄ ceramics was adapted from ref. 52. The appropriate amounts of La(NO₃)₃·6H₂O and Eu(NO₃)₃·6H₂O were weighed out gravimetrically and then dissolved in millipure H₂O with a resistivity of 18 MΩ. H₃PO₄ was then added in excess to this solution with stirring and a white precipitate formed, according to the equation 1:



The solution was heated at 90 °C for ~12 h to promote full conversion of the nitrate salts to the phosphate form. Then, the supernatant was decanted and the solid was split evenly into centrifuge tubes, suspended in millipure H₂O, and centrifuged for ~15 min. This process was repeated five times to remove impurities from the phosphate solid. After that, the solid was suspended in a 0.1 M HNO₃ acid wash as reported by ref. 52, and left to sit overnight. Then, the dilute acid was decanted off and the solid was transferred to an alumina crucible and dried in a furnace for three hours at 120 °C.

The solid was calcined at 500 °C for two hours, allowed to cool, and then ground in an agate mortar and pestle for approximately five minutes. The powder was split in 0.5 g amounts and pressed with an Oehlglass, Hahn, and Kolb MP12 uniaxial cold press with a force of 38 kN ($P = 450$ MPa) into green pellets 10 mm in diameter and with ~1 mm thickness. The green density of the pellets was calculated using the geometric method. Details of density and porosity measurements are given in the Supplementary information (SI), section *Density determination*, Supplementary Table 1.

Green pellets were placed in alumina crucibles, transferred to a tube furnace, and sintered at 1400 °C in air for four to five hours using a ramp rate of 4 °C/min and a cooling rate of 6 °C/min.

Synthesis of LaPO₄ single crystals. LaPO₄ single crystals were synthesized by a high-temperature solution (flux) method. The molar ratio of the flux components was 75:25:2 ≡ MoO₃:Li₂CO₃:LaPO₄. Homogeneity of the flux was ensured by holding the solution at 1173 K for 12 h before raising the temperature to 1623 K for complete dissolution of the monazite powder and subsequent cooling to 1143 K with 2 K/h for single crystal growth. Afterwards, the crucibles were removed from the furnace and cooled in air. The single crystals were extracted by dissolving the flux in water in an ultrasonic bath. All experiments were carried out in closed platinum crucibles.

Instrumental methods

Grazing-incidence X-Ray diffraction. GIXRD synchrotron radiation diffraction data were collected at the Rossendorf Beamline (ROBL BM20³⁸) at the European Synchrotron Radiation Facility (ESRF, Grenoble, France). For this, a dedicated GI module available at ROBL was employed. This module allows a full alignment of the studied pellets with respect to the incident synchrotron beam with a subsequent data acquisition at desired grazing angles, α . Details of the sample alignment procedure and data collection can be found in ref. 39. During data collection studied here monazite samples were rotated by 20° in order to improve peak shape and statistics of samples with coarse grain structure.

Diffraction setup was calibrated using a NIST 660c LaB₆ powder. The experiment energy of the incoming synchrotron radiation was set to 12 keV and beam was focalized and slitted down to a 0.4 mm (horizontal) and 0.03 mm (vertical) size. Data were recorded on a Pilatus 2M detector and reduced to one-dimensional powder patterns with PyFAI⁵³ and Dioptas⁵⁴ packages.

Vertical scanning interferometry. VSI data were obtained by means of an SNeox 3D Optical Profiler (Sensofar, Spain) with 10× and 100× Mirau objectives (1.3 and 0.13 μm/pixel, respectively) in the white-light mode, at a vertical resolution of ~1 nm. The topography datasets were processed using the imaging software SPIP (version 6.7.4, Image Metrology, Denmark).

Scanning electron microscopy. To avoid altering the irradiated surface, samples were not sputtered or treated before analysis. Microstructural characterization was performed by SEM and EDS (FESEM Gemini 500, Zeiss, Oberkochen, Germany; EDS detector X-Max80, Oxford Instruments, Abingdon, Oxfordshire, UK). Acceleration voltages of 1 kV yielded high-quality secondary electron images without surface charging. However, backscattered images had to be taken at 15 kV in the variable pressure mode. The reduced vacuum allows charge equalization at the surface by the gas molecules.

Raman spectroscopy. Raman spectra were collected on a Horiba Jobin Yvon Raman spectrometer equipped with an Olympus BX41 optical microscope in a non-confocal setup. Spectra were obtained using a He/Ne laser ($\lambda = 633$ nm) excitation source. The beam diameter was ~1 μm. Typical parameters for the collection of spectra included 20 s acquisition time and 10 accumulations over the range of 70–1200 cm⁻¹. Cosmic ray removal was applied. Background corrections and peak fitting were conducted using the OriginPro software package. A pseudo-Voigt fitting scheme was used to determine the peak centers and FWHM values.

Luminescence spectroscopy. To achieve the required spectra resolution, solid samples were cooled to ~10 K in a helium-refrigerated cryostat. TRIFS for the collection of Eu(III) excitation and emission spectra was performed with a pulsed Nd:YAG (Continuum, Surelite) pumped dye laser setup (Radiant Dyes Narrow Scan K) by directly exciting the Eu(III) ion from the ground state (⁷F₀) to the emitting state (⁵D₀). The emitted luminescence was directed into an optical multichannel analyzer (Shamrock 303i) with a 1200 lines/millimeter grating and the emission was detected with an intensified CCD camera (iStar, Andor) 1 μs, 1 ms, and 5 ms after the exciting laser pulse in a time window of 10 ms. The laser pulse energy and the exact excitation wavelength were monitored with an optical power meter (Newport 1918-R) and a wavelength meter (High Finesse WS-5), respectively.

Excitation Spectra were integrated over the F₂ band and normalized to allow for comparisons in peak center and FWHM.

Irradiation details

Irradiations were performed at the Ion Beam Center at the Helmholtz-Zentrum Dresden-Rossendorf, Germany (HZDR) using the 3 MV Tandem Ion Implanter. Samples were secured to a Si wafer which was then mounted in the implantation chamber, evacuated to ~3 × 10⁻⁷ mbar, and cooled to liquid nitrogen temperature (77 K). This was done to prevent structural annealing due to heating of the sample surface upon irradiation because the critical amorphization temperatures of monazites are rather low⁹. Samples were irradiated with 14 MeV Au⁵⁺ ions to fluences of 5 × 10¹³, 1 × 10¹⁴, and 1 × 10¹⁵ ions/cm². Calculations using the SRIM²⁹ software predict a penetration depth of the Au-ions of ~2 μm into the LaPO₄ monazite ceramics (theoretical density = 5.08 g/cm³). Displacements per atom are reported in Supplementary Table 2. The SRIM full cascade and cumulative displacements calculations are presented in Supplementary Fig. 1 and Supplementary Fig. 2, respectively.

Data availability

The datasets from this study are available from the authors upon reasonable request.

Received: 18 March 2024; Accepted: 7 August 2024;

Published online: 19 August 2024

References

- Clavier, N., Podor, R. & Dacheux, N. Crystal chemistry of the monazite structure. *J. Eur. Ceram. Soc.* **31**, 941–976 (2011).
- Kanazawa, Y. & Kamitani, M. Rare earth minerals and resources in the world. *J. Alloy. Compd.* **408–412**, 1339–1343 (2006).
- Boatner, L. A. Synthesis, structure, and properties of monazite, pretulite, and xenotime. *Rev. Mineral. Geochem.* **48**, 87–121 (2002).
- Dacheux, N., Clavier, N. & Podor, R. Versatile Monazite: Resolving geological records and solving challenges in materials science. Monazite as a promising long-term radioactive waste matrix: Benefits of high-structural flexibility and chemical durability. *Am. Mineral.* **98**, 833–847 (2013).
- Ni, Y., Hughes, J. M. & Mariano, A. N. Crystal chemistry of the monazite and xenotime structures. *Am. Mineral.* **80**, 21–26 (1995).
- Qin, D. et al. Incorporation of thorium in the rhabdophane structure: synthesis and characterization of Pr_{1-2x}CaxThxPO₄·nH₂O solid solutions. *J. Nucl. Mater.* **492**, 88–96 (2017).
- Nasdala, L. et al. The absence of metamictisation in natural monazite. *Sci. Rep.* **10**, 14676 (2020).
- Gramaccioli, C. M. & Segalstad, T. V. Uranium- and thorium-rich monazite from a south-alpine pegmatite at Piona, Italy. *Am. Mineral.* **63**, 7/8 (1978).
- Meldrum, A., Boatner, L. A. & Ewing, R. C. Displacive radiation effects in the monazite- and zircon-structure orthophosphates. *Phys. Rev. B* **56**, 13805–13814 (1997).
- Weber, W. J. et al. Radiation effects in crystalline ceramics for the immobilization of high-level nuclear waste and plutonium. *J. Mater. Res.* **13**, 1434–1484 (1998).
- Ewing, R. C. Nuclear waste forms for actinides. *Proc. Natl Acad. Sci.* **96**, 3432–3439 (1999).
- Ewing, R. C. & Wang, L. Phosphates as nuclear waste forms. *Rev. Mineral. Geochem.* **48**, 673–699 (2002).
- Picot, V. et al. Ion beam radiation effects in monazite. *J. Nucl. Mater.* **381**, 290–296 (2008).
- Ruschel, K. et al. A Raman spectroscopic study on the structural disorder of monazite-(Ce). *Mineral. Petrol.* **105**, 41–55 (2012).
- Deschanel, X. et al. Swelling induced by alpha decay in monazite and zirconolite ceramics: A XRD and TEM comparative study. *J. Nucl. Mater.* **448**, 184–194 (2014).
- Rafiuddin, M. R. & Grosvenor, A. P. Probing the effect of radiation damage on the structure of rare-earth phosphates. *J. Alloy. Compd.* **653**, 279–289 (2015).
- Nasdala, L. et al. Irradiation effects in monazite-(Ce) and zircon: Raman and photoluminescence study of Au-irradiated FIB foils. *Phys. Chem. Miner.* **45**, 855–871 (2018).
- Popa, K. et al. Synthesis, characterization, and stability of americium phosphate, AmPO₄. *Inorg. Chem.* **59**, 6595–6602 (2020).
- Burakov, B. E., Garbuzov, V. M., Kitsay, A. A., Yagovkina, M. A. & Zirlin, V. A. Self-irradiation of monazite ceramics: contrasting behavior of PuPO₄ and (La,Pu)PO₄ doped with Pu-238. *MRS Proc.* **824**, CC4.1 (2004).
- Bregiroux, D., Belin, R., Valenza, P., Audubert, F. & Bernache-Assollant, D. Plutonium and americium monazite materials: solid state synthesis and X-ray diffraction study. *J. Nucl. Mater.* **366**, 52–57 (2007).
- Barr, C. M., El-Atwani, O., Kaoumi, D. & Hattar, K. Interplay between grain boundaries and radiation damage. *JOM* **71**, 1233–1244 (2019).
- Lu, F. et al. Size dependence of radiation-induced amorphization and recrystallization of synthetic nanostructured CePO₄ monazite. *Acta Material.* **61**, 2984–2992 (2013).
- Dey, S. et al. Radiation tolerance of nanocrystalline ceramics: insights from yttria stabilized zirconia. *Sci. Rep.* **5**, 7746 (2015).
- Jiang, H., Wang, X. & Szlufarska, I. The multiple roles of small-angle tilt grain boundaries in annihilating radiation damage in SiC. *Sci. Rep.* **7**, 42358 (2017).
- Seydoux-Guillaume, A.-M., Montel, J.-M., Wirth, R. & Moine, B. Radiation damage in diopside and calcite crystals from uranothorianite inclusions. *Chem. Geol.* **261**, 318–332 (2009).
- Nasdala, L., Grötzschel, R., Probst, S. & Bleisteiner, B. Irradiation damage in monazite-(Ce): an example to establish the limits of raman confocality and depth resolution. *Can. Mineral.* **48**, 351–359 (2010).
- Begun, G. M., Beall, G. W., Boatner, L. A. & Gregor, W. J. Raman spectra of the rare earth orthophosphates. *J. Raman Spectrosc.* **11**, 273–278 (1981).
- Silva, E. N. et al. Vibrational spectra of monazite-type rare-earth orthophosphates. *Opt. Mater.* **29**, 224–230 (2006).
- Ziegler, J. F., Ziegler, M. D. & Biersack, J. P. SRIM – The stopping and range of ions in matter (2010). *Nucl. Instrum. Methods Phys. Res. Sect. B Beam Interact. Mater. At.* **268**, 1818–1823 (2010).
- Stoller, R. E. et al. On the use of SRIM for computing radiation damage exposure. *Nucl. Instrum. Methods Phys. Res. Sect. B Beam Interact. Mater. At.* **310**, 75–80 (2013).
- Miotello, A. & Kelly, R. Revisiting the thermal-spike concept in ion-surface interactions. *Nucl. Instrum. Methods Phys. Res. Sect. B Beam Interact. Mater. At.* **122**, 458–469 (1997).
- Vineyard, G. H. Thermal spikes and activated processes. *Radiat. Eff.* **29**, 245–248 (1976).
- Zhang, Y. et al. Grain growth and phase stability of nanocrystalline cubic zirconia under ion irradiation. *Phys. Rev. B* **82**, 184105 (2010).
- Benyagoub, A. Mechanism of the monoclinic-to-tetragonal phase transition induced in zirconia and hafnia by swift heavy ions. *Phys. Rev. B* **72**, 094114 (2005).
- Ingerle, D., Pepponi, G., Meirer, F., Wobruschek, P. & Strelci, C. JGIXA – A software package for the calculation and fitting of grazing incidence X-ray fluorescence and X-ray reflectivity data for the characterization of nanometer-layers and ultra-shallow-implants. *Spectrochim. Acta Part B At. Spectrosc.* **118**, 20–28 (2016).
- Henke, B. L., Gullikson, E. M. & Davis, J. C. X-ray interactions: photoabsorption, scattering, transmission, and reflection at E = 50–30,000 eV, Z = 1–92. *At. Data Nucl. Data Tables* **54**, 181–342 (1993).
- Van Den Hoogenhof, W. W. & De Boer, D. K. G. Glancing-incidence X-ray analysis. *Spectrochim. Acta Part B At. Spectrosc.* **48**, 277–284 (1993).
- Scheinost, A. C. et al. ROBL-II at ESRF: a synchrotron toolbox for actinide research. *J. Synchrotron Radiat.* **28**, 333–349 (2021).
- Svitlyk, V. et al. Grazing-incidence synchrotron radiation diffraction studies on irradiated Ce-doped and pristine Y-stabilized ZrO₂ at the Rossendorf beamline. *J. Synchrotron Rad.* **31**, 355–362 (2024).
- Juhás, P., Davis, T., Farrow, C. L. & Billinge, S. J. L. PDFgetX3: a rapid and highly automatable program for processing powder diffraction data into total scattering pair distribution functions. *J. Appl. Crystallogr.* **46**, 560–566 (2013).
- Fischer, C., Finkeldei, S., Brandt, F., Bosbach, D. & Lüttge, A. Direct measurement of surface dissolution rates in potential nuclear waste forms: the example of pyrochlore. *ACS Appl. Mater. Interfaces* **7**, 17857–17865 (2015).
- Fischer, C., Kurganskaya, I., Schäfer, T. & Lüttge, A. Variability of crystal surface reactivity: what do we know? *Appl. Geochem.* **43**, 132–157 (2014).
- Meldrum, A., Boatner, L. A., Weber, W. J. & Ewing, R. C. Radiation damage in zircon and monazite. *Geochim. Cosmochim. Acta* **62**, 2509–2520 (1998).
- Zhang, Y. & Weber, W. J. Ion irradiation and modification: the role of coupled electronic and nuclear energy dissipation and subsequent nonequilibrium processes in materials. *Appl. Phys. Rev.* **7**, 041307 (2020).

45. Kalita, P. et al. Grain size effect on the radiation damage tolerance of cubic zirconia against simultaneous low and high energy heavy ions: nano triumphs bulk. *Sci. Rep.* **11**, 10886 (2021).
 46. Becker, M., Scheel, H., Christiansen, S. & Strunk, H. P. Grain orientation, texture, and internal stress optically evaluated by micro-Raman spectroscopy. *J. Appl. Phys.* **101**, 063531 (2007).
 47. Lalla, E. A. et al. Structural and vibrational analyses of CePO₄ synthetic monazite samples under an optimized precipitation process. *J. Mol. Struct.* **1223**, 129150 (2021).
 48. Binnemans, K. Interpretation of europium(III) spectra. *Coord. Chem. Rev.* **295**, 1–45 (2015).
 49. Huittinen, N., Arinicheva, Y., Schmidt, M., Neumeier, S. & Stumpf, T. Using Eu³⁺ as an atomic probe to investigate the local environment in LaPO₄–GdPO₄ monazite end-members. *J. Colloid Interface Sci.* **483**, 139–145 (2016).
 50. Huittinen, N. et al. Probing structural homogeneity of La_{1-x}Gd_xPO₄ monazite-type solid solutions by combined spectroscopic and computational studies. *J. Nucl. Mater.* **486**, 148–157 (2017).
 51. Wang, X. et al. Radiation-induced segregation in a ceramic. *Nat. Mater.* **19**, 992–998 (2020).
 52. Babelot, C., Bukaemskiy, A., Neumeier, S., Modolo, G. & Bosbach, D. Crystallization processes, compressibility, sinterability and mechanical properties of La-monazite-type ceramics. *J. Eur. Ceram. Soc.* **37**, 1681–1688 (2017).
 53. Kieffer, J. & Karkoulis, D. PyFAI, a versatile library for azimuthal regrouping. *J. Phys. Conf. Ser.* **425**, 202012 (2013).
 54. Prescher, C. & Prakapenka, V. B. DIOPTAS: a program for reduction of two-dimensional X-ray diffraction data and data exploration. *High. Press. Res.* **35**, 223–230 (2015).
- data curation, formal analysis, review, and editing; M.H.: methodology, review, and editing; S.A.: methodology, review, and editing; C.H.: methodology, review, supervision, and editing; B.W. review and editing, funding acquisition; T.T.: review; L.P.: review and editing; C.F.: methodology, review, and editing; N.H.: conceptualization, funding acquisition, project administration, resources, supervision, writing, review, and editing.

Funding

Open Access funding enabled and organized by Projekt DEAL.

Competing interests

The authors declare no competing interests.

Additional information

Supplementary information The online version contains supplementary material available at <https://doi.org/10.1038/s41529-024-00504-3>.

Correspondence and requests for materials should be addressed to Sara E. Gilson or Nina Huittinen.

Reprints and permissions information is available at <http://www.nature.com/reprints>

Publisher's note Springer Nature remains neutral with regard to jurisdictional claims in published maps and institutional affiliations.

Open Access This article is licensed under a Creative Commons Attribution 4.0 International License, which permits use, sharing, adaptation, distribution and reproduction in any medium or format, as long as you give appropriate credit to the original author(s) and the source, provide a link to the Creative Commons licence, and indicate if changes were made. The images or other third party material in this article are included in the article's Creative Commons licence, unless indicated otherwise in a credit line to the material. If material is not included in the article's Creative Commons licence and your intended use is not permitted by statutory regulation or exceeds the permitted use, you will need to obtain permission directly from the copyright holder. To view a copy of this licence, visit <http://creativecommons.org/licenses/by/4.0/>.

© The Author(s) 2024

Acknowledgements

We acknowledge the use of the Ion Beam Center, HZDR for irradiations and the use of ROBL for GIXD measurements. We gratefully acknowledge the BMBF for funding through grant number 02NUK060.

Author contributions

S.E.G.: investigation, formal analysis, methodology, data curation, writing, review, and editing; V.S.: formal analysis, data curation, writing, review, and editing; A.A.K.: methodology, data curation, review, and editing; J.N.: formal analysis, methodology, writing, review, and editing; T.L.: methodology, review, and editing; G.L.M.: methodology, review, supervision, and editing; H.L.: formal analysis, data curation, review, and editing; J.M.: investigation,